Nonlinear phononic control and emergent magnetism in Mott insulating titanates

Mingqiang Gu and James M. Rondinelli

Phys. Rev. B **98**, 024102 — Published 9 July 2018

DOI: 10.1103/PhysRevB.98.024102

Nonlinear Phononic Control and Emergent Magnetism in Mott Insulating Titanates

Mingqiang Gu[1] and James M. Rondinelli[1, *]

[1] *Department of Materials Science and Engineering,*
Northwestern University, Evanston, Illinois 60208, USA

Optical control of structure-driven magnetic order offers a platform for magneto-optical terahertz devices. We control the magnetic phases of d^1 Mott insulating titanates using nonlinear phononics to transiently perturb the atomic structure based on density functional theory (DFT) simulations and solutions to a lattice Hamiltonian including nonlinear multimode interactions. We show that magnetism is tuned by indirect excitation of a Raman-active phonon mode, which affects the amplitude of the TiO_6 octahedral rotations that couple to static Ti–O Jahn-Teller distortions, through driven infrared-active modes of $LaTiO_3$ and $YTiO_3$. The mode excitation reduces the rotational angle, driving a magnetic phase transition from a ferromagnetic (FM) to G-type antiferromagnetic (AFM) state. A novel A-type AFM state hidden in the bulk equilibrium phase diagram emerges as a dynamically accessible optically induced phase under multimode excitations. Our work shows that nonlinear phononics can stabilize phases inaccessible to static chemical substitutions or lattice strains.

I. INTRODUCTION

Recent advances in laser sciences enable light pulses to selectively pump phonon modes in crystals as a means to manipulate the transient atomic structure and structure-derived properties of materials. Ultrafast phononic control provides an alternative route beyond static methods, i.e. chemical pressure and thin film strain, to access nonequilibrium quantum states.[1,2] By exciting an infrared-active (IR) mode so intensely that it induces a displacive force to a Raman mode through a nonlinear phononic (NLP) interaction, the charge-ordering state in manganites has been melted,[3] the superconducting temperature in cuprate and fullerene systems has been increased,[4,5] and the direction of the electric polarization in a ferroelectric has been flipped[6]—all processes on the picosecond time scale. Recent work has also shown that a two-mode excitation approach may be used to control the direction of a targeted distortion using polarized light,[7] broadening the prospect of ultrafast structural manipulation.

In addition to well-defined electronic and dielectric states, the magnetic order in complex transition metal oxides are exceedingly sensitive to subtle changes in atomic structure. Indeed, control over atomic structure through strain engineering or compositional changes can produce new ferroic states in manganites,[8,9] ruthenates,[10] and titanates;[11] however, structure-induced magnetic phase transitions in complex ternary oxides remain to be designed using NLP control, i.e. magnetophononics,[12,13] to enable dynamical multiferroism.[14,15] The main concept is to use light to exploit the structure-magnetic state dependencies originating in microscopic metal-oxygen-metal bond angles and metal-oxygen bond lengths.[16] In this sense, effective magnetic fields can be elicited through pure phononic excitation.[17]

Ultrafast phononic structure control arises from the nonlinear terms in the Hamiltonian expressed as a function of the amplitudes of Raman-active (A_g) and IR-active phonon (B_u) modes:[18]

$$E = \frac{1}{2}\nu_R^2 Q_R^2 + \frac{1}{2}\nu_{IR}^2 Q_{IR}^2 + \frac{1}{3}a_3 Q_R^3 + \frac{1}{4}b_4 Q_{IR}^4 + g Q_R Q_{IR}^2 + \dots , \tag{1}$$

where $\nu_{R,IR}$ and $Q_{R,IR}$ are the frequencies and amplitudes of the Raman and IR modes, respectively. The vibrational center of the Raman mode, which strongly affects macroscopic properties in oxides owing to changes in bond angles and lengths, is displaced by the IR mode through the nonlinear term $\sim Q_R Q_{IR}^2$. By coherently pumping the IR mode, one is able to manipulate the material properties on the $10 \sim 100$ picosecond timescale.

Titanates with one electron occupying the d orbital (d^1) are an ideal family to explore structure-dependent electronic and magnetic properties.[19] Both $LaTiO_3$ and $YTiO_3$ are Mott insulators;[20] however, they exhibit different magnetic-[21] and orbital-[19,22] ordered states. $LaTiO_3$ (LTO) is a G-type antiferromagnet (AFM) with a Néel temperature $T_N = 150$ K while $YTiO_3$ (YTO) is an unusual ferromagnetic (FM) insulator with a Curie temperature $T_C = 30$ K. The appearance of both FM and AFM spin configurations indicates the d^1 system is not a simple Mott insulator. The differences in ordering temperatures can be understood using the Kugel-Khomskii rule,[23] which states that the d^1 magnetic state is coupled to the orbital degeneracy lifting within the t_{2g} manifold, which is highly sensitive to the lattice distortion. Prior theoretical studies have reproduced the correct magnetic ground states[24] and identified how their stability depends on lifting of the $3d\, t_{2g}$ orbital degeneracy, which is linked to the amplitude of the in-phase and out-of-phase TiO_6 octahedral rotations.[19] Such octahedral rotations are enhanced in YTO owing to the small Y cation size. The magnetic ordering has been shown theoretically to be tunable with strain;[25] however, there is no experimental demonstration of the change in magnetism. Importantly, the A-type AFM state is unreported in any known d^1 titanate with trivalent A site cations.

In this work, we describe a protocol to manipulate

TABLE I. Calculated unit cell parameters for $LaTiO_3$ and $YTiO_3$. Data provided for orthorhombic $LaTiO_3$ ($Pbnm$, space group 62, setting 3) using the PBEsol+U_{eff} functional compared to experiment. The tilt (ϕ)and rotation (θ) angles are also listed.

	$LaTiO_3$			$YTiO_3$		
	U_{eff}=0 eV	U_{eff}=4.4 eV	Ref. [34]	U_{eff}=0 eV	U_{eff}=4.4 eV	Ref. [21]
a (Å)	5.50	5.65	5.6301	5.27	5.35	5.335
b (Å)	5.59	5.67	5.5844	5.66	5.73	5.684
c (Å)	7.85	7.92	7.901	7.58	7.61	7.615
ϕ (°)	13.07	15.42	12.74	20.01	21.71	20.12
θ (°)	9.53	10.56	9.17	12.02	13.08	12.51

the magnetic order in ternary oxides through ultrafast dynamical structure control. The prerequisite for such control relies on selection of an equilibrium material with its magnetic phase stability dependent upon a cooperative atomic displacive mode that resembles a natural Raman-active mode of the crystal, e.g., rotations of octahedra. The sensitivity of the phase stability is assessed through local pertubations to the atomic structure, and then the Raman mode that most resembles the local atomic distortion is targeted for mode-selective pumping through the NLP interactions. We demonstrate this process for the Mott insulating titanates and show that the NLP interactions provide access to both ferromagnetism (FM) and antiferromagnetism (AFM), including a layered A-type AFM absent from the equilibrium titanate phase diagram. Although this phase has been theoretically predicted to be accessible with strain engineering,[25] it remains to be observed in experiment and may be easier to achieve dynamically as proposed herein. Finally, we show the critical laser intensity to drive the transitions can be tuned with thin film epitaxy, motivating nonlinear magnetophononics experiments on thin film titanates.

The Article is organized as follows: In Sec. II we describe the methodology used to calculate the atomic and electronic structure and lattice dynamical properties. In Sec. III we present our main results focusing on equilibrium structure-property relationship which are exploited to realize magnetophononics and a magnetic transition, selection of the target mode for excitation, and the nonlinear phononic process that excites the downselected mode. We then discuss challenges associated with our proposal and possible routes to realized the magnetic transition in Sec. IV. We conclude in Sec. V.

II. METHODS

A. Computational Details

Density functional theory (DFT) calculations were performed with the Vienna Ab-initio Simulation Package (VASP)[26,27] with the projector augmented wave (PAW) method[28] to treat the core and valence electrons using the following electronic configurations: $4s^2 4p^6 5s^2 4d^1$ for Y, $6s^2 5s^2 5p^6 5d^1$ for La, $3s^2 3p^6 3d^2$ for Ti, and $2s^2 2p^4$ for O. The revised Perdew-Burke-Ernzerhof (PBE) exchange-correlation functional for solids (PBEsol)[29] was selected as it gives accurate oxide lattice parameters. The Brillouin zone is sampled using an $8 \times 8 \times 6$ Γ-centered Monkhorst-Pack k-point mesh and integrations are performed using Gaussian smearing with a width of 10 meV. All structures were restricted to the observed $Pbnm$ symmetry during structural optimization, whereby the lattice constants and atomic positions are relaxed until the stresses and forces on each atom are less than 60 μeV Å^{-3} and 0.1 meV Å^{-1}, respectively. The lattice dynamical properties are computed using the frozen phonon method, which is implemented in PHONOPY.[30]

Owing to the correlated Ti-3d electrons, we used the plus Hubbard U method of Dudarev *et al.*[31] In this approach, only a $U_{\mathrm{eff}} = U - J$ is considered and we select $U_{\mathrm{eff}} = 4.4$ eV, which reproduces the Mott insulating phases for both LTO and YTO. The selection of this U_{eff} value is based on previous constrained-LDA calculations.[32] Structurally $U_{\mathrm{eff}} = 4.4$ eV more closely reproduces the orthorhombicity a/b value (0.997) for $LaTiO_3$ from experiment (1.008). Electronically, the U_{eff} value overestimates the band gap for both materials, i.e., ∼1.9 eV for $LaTiO_3$ and ∼2.2 eV for $YTiO_3$. Nonetheless, previous DMFT+U calculations with similar U values obtained accurate spectral functions for the titanates (compared to the experiment).[19] More importantly, although the exchange interactions J depend on the quantitative value of U, our selected U_{eff} reproduces the correct magnetic order for both $LaTiO_3$ (G-AFM) and $YTiO_3$ (FM). Since our previous study shows that the U-dependence of the linear and nonlinear phononic properties is negligible,[33] our calculations with this parameter are reasonably justified. In addition, the theoretical optimized structure parameters are listed in Table I and we find sufficient agreement between the DFT-PBEsol+U_{eff} values and experiment.

B. Exchange Interactions

The exchange coupling J_{ij} between nearest neighboring Ti ions at site i and j is computed using the four-state method[35] as

$$J_{ij} = \frac{E_{\uparrow\uparrow} + E_{\downarrow\downarrow} - E_{\uparrow\downarrow} - E_{\downarrow\uparrow}}{4} \,,$$

TABLE II. The exchange coupling constants between nearest in-plane (J_i) and out-of-plane (J_o) Ti atoms evaluated with different values of electron correlation $U_{\rm eff}$.

	LaTiO$_3$			YTiO$_3$		
$U_{\rm eff}$	J_i	J_o	state	J_i	J_o	state
0	-0.1	0.0	FM	-28.9	-16.8	FM
3.2	3.0	2.7	*G*-AFM	-1.5	1.5	*A*-AFM
4.4	1.9	3.9	*G*-AFM	-3.5	-1.9	FM

where the energies are computed with DFT and the spin at the neighboring sites are aligned as denoted by the four different states in the expression above. The spin for all the other Ti sites are fixed according to the original ground state, i.e., FM for YTO and *G*-AFM for LTO. The estimated $|J|$ values for the two titanates are of the same order (Table II), which is inconsistent with the experimental observation that the magnetic ordering temperature differs by a factor of five. Our magnetic ordering temperature estimated with the computed exchange coupling constants ($U_{\rm eff} = 4.4$ eV) are 52 K for YTO and 46 K for LTO within the mean field limit. The deviation from experimental values is partially due to the U dependence of the computed exchange interactions and subtle different orbital physics as elaborated on next.

The reason for this DFT shortcoming arises from the U dependence on the computed J values. Solovyev[36] found that there is no unique U parameter that can predict correctly the magnetic ground state for both YTO and LTO at the LDA+U level. This problem is partially solved by using the PBEsol+U functional, i.e., it is possible to find a unique U value that can reproduce the correct ground state for both materials; however, the computed J values are still U-dependent (Table II). Therefore the discrepancy between the DFT predicted and experimental J values is expected. A prior study has tried to understand the physical origin for this discrepancy and suggest that is arises from the different orbital physics active in these two oxides. Indeed, the exchange interactions computed for different orbital projections in the two materials shows a difference in magnitude of ∼5 times.[19]

III. RESULTS

A. Structure-property relationships

We first analyze the relationship between the orthorhombic structure parameters and the magnetic order using first-principles calculations based on density functional theory (DFT). Both LTO and YTO exhibit *Pbnm* symmetry whereby neighboring TiO$_6$ octahedra rotate in-phase about the c axis ($a^0a^0c^+$) and tilt out-of-phase about the pseudocubic [110] direction ($a^-a^-c^0$ tilt pattern). Our calculated structure parameters for both titanates are in good agreement with the experimental data, including the tilting ϕ and rotation θ angles as defined in Ref. 37. Because Y exhibits a smaller cation radius than La, the unit cell volume for YTO is 8% smaller than that of LTO. One consequence of this is that the Goldschmidt tolerance factor $\tau = (r_{\rm A} + r_{\rm O})/[\sqrt{2}(r_{\rm B} + r_{\rm O})]$ is smaller for YTO than LTO (and both are smaller than 1). Thus, the rotation and tilt angles in YTO are larger than those in LTO. The change in magnitude of the octahedral rotation amplitudes in the equilibrium structures affects the effective exchange coupling between neighboring Ti ions through superexchange interactions. If the total exchange coupling for nearest neighbors is written as $J = J_0 + J_{\rm SX}$, where $J_0 < 0$ is the direct exchange coupling between two ions and $J_{\rm SX}$ is the superexchange between the two Ti ions bridged by an oxide ion, then according to the Goodenough-Kanamori-Anderson rules, $J_{\rm SX}$ should be positive for the d^1 system, which favors an AFM spin configuration. Furthermore, the magnitude of superexchange $|J_{\rm SX}| \propto (1 - \cos\angle({\rm Ti-O-Ti'}))$, decreases as the $\angle({\rm Ti-O-Ti'})$ deviates from 180°. Therefore when the rotational distortions increase, the spin system will favor a FM configuration, and vice versa. These aforementioned exchange dependencies on the octahedral rotation angles reflect the origin of the bulk equilibrium magnetic phases.

The change in TiO$_6$ rotation amplitudes in the equilibrium structures also affects the t_{2g} orbital degeneracy. Based on the three-center superexchange model within the configuration-interaction scheme,[38] the naturally active orbital for the FM and AFM states are different, which alters the effective exchange coupling between neighboring Ti cations. To validate the structural origin of the magnetic configurations, we performed DFT calculations on hypothetical structures that follow an adiabatic trajectory connecting the LTO and YTO structures. Along this trajectory both chemical compositions are used to compute the difference in total energy between the known FM and *G*-AFM spin orders (Fig. 1a). Formally, we define ζ as the independent structural parameter in the trajectory, such that $\zeta = 0$ ($\zeta = 1$) denotes the equilibrium LTO (YTO) structure. Structures between $\zeta = 0$ and 1 are obtained as a linear interpolation between the two end members, i.e. $x_\zeta(i) = x_0(i) + \zeta dx(i)$, in which $x(i)$ is the fractional coordinate for atom i and $dx(i) = x_1(i) - x_0(i)$. We find for both compounds that independent of the La or Y chemistry, if the titanate exhibits the LTO crystal structure ($\zeta = 0$) than the *G*-AFM state is always favored. As ζ increases away from zero in the LTO structure towards that of YTO, a magnetic transition occurs at $\zeta \sim 0.15$ for Y and $\zeta \sim 0.3$ for La. At these values the FM state is energetically favored.

Microscopically, these changes in magnetic states are due to changes in the effective exchange coupling J. To identify the different contributions from the rotation and tilt distortions, which are related to the equatorial or apical oxide anions connecting the two Ti cations, respectively, we computed the in-plane (J_i) and out-of-plane (J_o) exchange constants between nearest Ti sites (Fig. 1b) using the aforementioned four-state method.[35] It is clear that the signs for both J_i and J_o change from positive

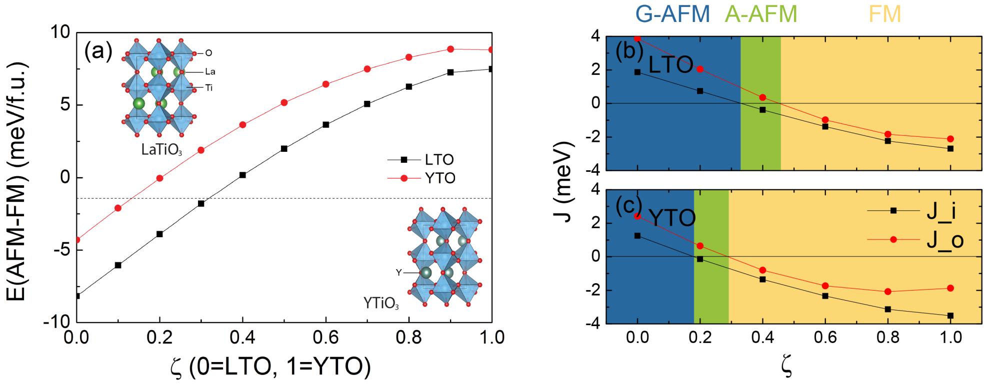

FIG. 1. (Color online) (a) Energy difference between FM and G-AFM phase as a function of ζ. (b,c) The exchange coupling constants between nearest in-plane (J_i) and out-of-plane (J_o) Ti atoms as functions of ζ in LTO and YTO. Different shaded regions in (b) and (c) denote the evolution in stable magnetic phase. The insets in (a) show the structure of LTO and YTO.

(AFM coupling) to negative (FM coupling) as the structure evolves from that of LTO to YTO. The critical ζ for the in-plane coupling is about 0.2 while that for the out-of-plane is ~ 0.3 in YTO. These critical values shift to higher ζ for LTO and are consistent with the phase diagram given in Fig. 1. Interestingly, our analysis shows that for YTO (LTO) there should be an additional A-type AFM phase bridging the FM and G-AFM phases in the region of $0.2 < \zeta < 0.3$ ($0.3 < \zeta < 0.45$). The total energy for the A-AFM configuration at $\zeta = 0.25$ is about 0.5 meV more stable than that of the FM phase.

The critical rotation and tilt angles required to achieve the transition are smaller than the average structure ($\zeta = 0.5$). In LTO these angles are $\theta = 11.4°$, $\phi = 17.5°$ (FM to A-AFM) and $\theta = 11.7°$, $\phi = 18.3°$ (A-AFM to G-AFM), respectively, which are close to those for YTO: $\theta = 11.0°$, $\phi = 16.6°$ (FM to A-AFM) and $\theta = 11.3°$, $\phi = 17.3°$ (A-AFM to G-AFM), respectively. Therefore, we propose that control of the magnetic state in d^1 titanates should be possible through changes in the TiO$_6$ octahedral rotation and tilt angles. Since these rotational modes transform as the fully symmetric representation of point group mmm (D_{2h}), the next task is to identify the Raman mode that is optimally suited to participate in the NLP interaction.

B. Raman mode selection

The octahedral rotation and tilt can be changed by activating a Raman phonon mode. Using YTO as an example, the Raman mode that most effectively modulates the octahedral rotation amplitude should be identified. The (linear) phonon frequency and character for all 7 A_g modes and five highest frequency B_u modes for YTO are given in Table III.

According to the Born-Oppenheimer approximation, the separation of time scales between the electronic and the phononic processes allows us to treat the phonon-excited nonequilibrium state within the quasi-static approximation. By distorting the structure along the eigenvector(s) of the phonon normal mode(s), we computed the "transient" electronic and magnetic properties within the DFT framework. This treatment has been successfully applied in some materials.[18,39] With this approximation, we compute the energy difference (ΔE) between AFM and FM states at different amplitudes of the A_g modes and identify the critical mode amplitude for the magnetic transition when ΔE changes sign (Fig. 2).

TABLE III. Frequency ν (in cm^{-1}) and phonon character for the Raman- and select high frequency IR-active modes in YTiO$_3$. For the IR modes, the coupling coefficient g to the A_g (25) tilt mode is also provided (in units of eV/(Å$\sqrt{\text{amu}}$)^3). The Q$_2$ Jahn-Teller mode corresponds to Raman mode A_g (49).

Raman			IR			
Index No.	Character	ν	Index No.	Character	ν	$g[A_g(25), B_u]$
9	A_g	142	48	B_{1u}	511	-0.04
12	A_g	154	53	B_{3u}	532	0.02
20	A_g	262	54	B_{1u}	543	0.05
25	A_g	298	56	B_{2u}	554	0.008
40	A_g	419	57	B_{1u}	561	0.006
44	A_g	445				
49	A_g	512				

In order to identify the character of the phonon vibrational pattern, the eigen-displacements of the phonon modes are projected onto displacements corresponding to rigid rotations, tilts or pure Jahn-Teller (Q$_2$) distortions, respectively, by computing the product

$$S(\mathrm{N},\mathrm{D}) = |\sum_i e_i(N) \cdot e_i(\mathrm{D})| \,.$$

Here $e_i(N)$ denotes the eigen-displacement of atom i for the phonon mode with index number N, whereas D=R, T, or JT denotes the rotation, tilt or Jahn-Teller distortion, respectively. Since these displacements under $Pbnm$ symmetry do not form an orthonormal basis set, we use a renormalized $\mathsf{S}(\mathrm{D}) = S(\mathrm{D})/[S(\mathrm{R}) + S(\mathrm{T}) + S(\mathrm{JT})]$ to identify the main effect of the phonon mode. The calculated similarity values for the seven A_g modes are

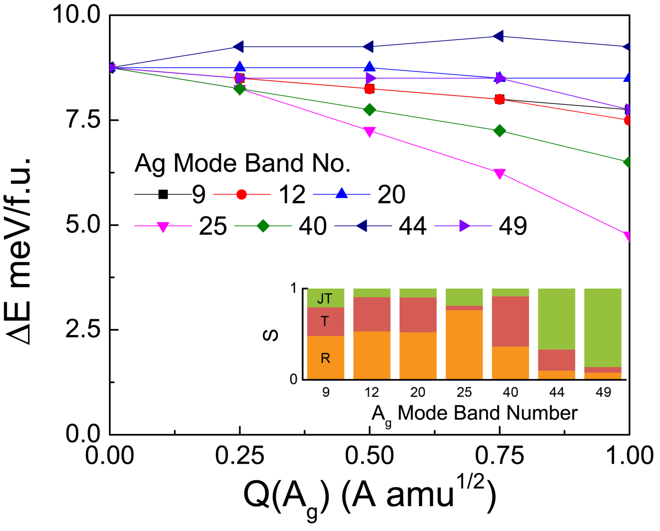

FIG. 2. The energy difference per formula unit (f.u.) between the FM and AFM phases as a function of the mode amplitude of the seven A_g Raman modes for YTiO$_3$. The inset shows the similarity (S) of each mode to the rigid rotation (R, orange), tilt (T, red) and pure Jahn-Teller (JT, green) distortions, respectively.

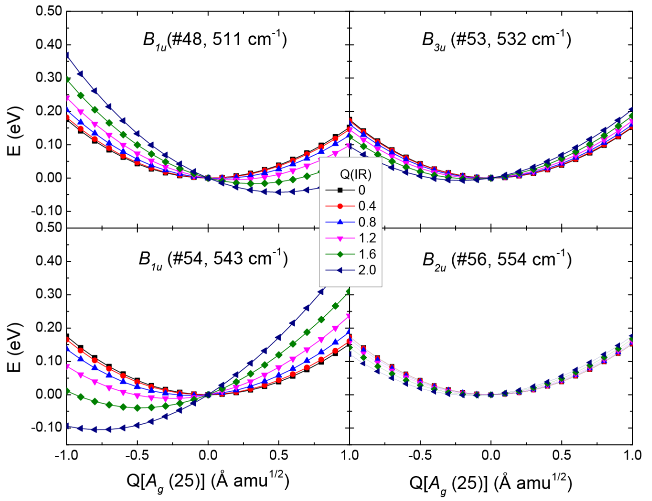

FIG. 3. Energy profiles for the nonlinear coupling between IR-active modes and the A_g (25) Raman mode in YTiO$_3$.

presented in the inset to Fig. 2. We conclude that the A_g (25) mode exhibits the largest octahedral rotation component and at the same time it is the most efficient mode to induce the FM to AFM transition.

Note that the phase diagram obtained by exciting the A_g (25) phonon mode shown in Fig. 2 differs from that obtained with respect to the structural parameter ζ (Fig. 1), because the Raman mode is not identical to ζ. The contributions of pure octahedral rotation, tilt and Jahn-Teller distortions differ between the A_g (25) phonon and ζ parameter; there is more rotation present in A_g (25).

Another interesting mode is the A_g mode with $\nu = 512$ cm^{-1} (index no. 49), an almost pure Jahn-Teller mode. Although this mode is not efficient in reducing the energy difference between the FM and G-AFM, the Q$_2$ Jahn-Teller mode is known to stabilize the A-AFM magnetic order in LaMnO$_3$,[40] and therefore may influence the stability of the A-AFM phase relative to the FM and G-AFM order if it is also excited.

C. Nonlinear phononics

We first identify which IR mode will couple strongest to the A_g(25) Raman mode. According to the theory of ionic Raman scattering, the amplitude of the Raman mode is largest when the frequency difference between the driven Raman mode and the pumped IR mode is maximized.[39] Therefore the coherently pumped IR mode should be a high frequency mode. We now examine the nonlinear coupling interactions between the five highest B_u IR-active modes to this Raman A_g (25) mode for bulk YTO. By fitting the energy surfaces $E(Q_\mathrm{R}, Q_\mathrm{IR})$ to Eq. 1, we obtained the coupling coefficients g, in Table III. We find four IR modes with a nonlinear coupling coefficient near or larger than 0.01 eV/(Å$\sqrt{\text{amu}}$)^3. The energy profiles for each of these modes with the A_g (25) mode are shown in Fig. 3. When the B_{1u} mode (index no. 48, $\nu = 511$ cm^{-1}) is pumped to an amplitude of 2 Å$\sqrt{\text{amu}}$, the A_g (25) mode finds its energy minimum at a nonequilibrium value $Q(A_g) \sim 0.5$ Å$\sqrt{\text{amu}}$. With the excitation of the B_{3u} mode (index no. 53, $\nu = 532$ cm^{-1}), the energy minimum of the A_g (25) mode is displaced by ~ -0.2 Å$\sqrt{\text{amu}}$. A similar strength excitation of another B_{1u} mode (index no. 54, $\nu = 543$ cm^{-1}) displaces the energy minimum by ~ -0.8 Å$\sqrt{\text{amu}}$. For the weakly coupled B_{2u} mode (index no. 56, $\nu = 554$ cm^{-1}), 2 Å$\sqrt{\text{amu}}$ excitation only shifts the energy minimum to approximately -0.1 Å$\sqrt{\text{amu}}$.

Among these IR modes, the nonlinear coupling coefficient for the B_{1u} (48) and the B_{1u} (54) are comparable. However, only the B_{1u} (48) mode shifts the energy minimum of the A_g (25) mode towards a larger amplitude, which is required to *reduce* the octahedral rotation angles and drive the magnetic transition. Therefore, this IR mode is selected to drive changes in the Raman mode through the NLP interaction. Note that the coefficient $g[A_g(25), B_{1u}(48)] \sim -0.039$ eV/(Å$\sqrt{\text{amu}}$)^3, which is three times larger in magnitude compared to the nonlinear phononic coupling strength in LaTiO$_3$.[33] This value is approximately one order of magnitude smaller than that reported in YBa$_2$Cu$_3$O$_7$[41] and about half of that found in PrMnO$_3$.[18]

Next, we obtain the time evolution of the phonon modes during this process by solving the equations of motion:

$$\begin{aligned} \ddot{Q}_{IR} + \nu_{IR}^2 Q_{IR}^2 &= F(t) - 2gQ_RQ_{IR}\,, \\ \ddot{Q}_R + \nu_R^2 Q_R^2 &= -2gQ_{IR}^2\,, \end{aligned} \tag{2}$$

where $F(t) = CF_0 \cos(\omega t) e^{-t/2\sigma^2}$ is the driving force applied by the laser pulse with a frequency of ω and a Gaussian shape envelope with a temporal width of σ. The

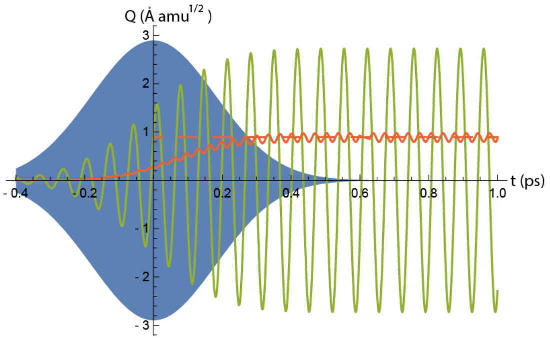

FIG. 4. Time evolution of the $A_g\,(25)$ mode (red) and the $B_{1u}\,(48)$ mode (green). The laser pulse envelope is schematically shown as the blue filled-curve. The dashed line denotes the displacive vibrational center of the $A_g\,(25)$ mode after pumped by a laser pulse with $\omega = 14.5$ THz and $I = 18$ MV/cm (damping is neglected).

factor $C = Z^*/\sqrt{m}$ is required to convert the unit of force into $\text{Å}\sqrt{\text{amu}}\cdot\text{ps}$, with Z^* being the Born effective charge of the mode ($0.83e$) and m the atomic mass unit.

For efficient mode pumping, the laser frequency should be in a resonant condition with the IR mode. Note that it is important to consider the red-shift of the IR mode in the nonlinear process under high laser intensity;[41] therefore, we propose the laser frequency of $\omega = 14.5$ THz. With a laser intensity of 18 MV/cm, the time evolution of the $A_g\,(25)$ and $B_{1u}(48)$ modes are plotted in Fig. 4. Although the maximum displacement of the $A_g\,(25)$ mode is $\sim 0.9\,\text{Å}\sqrt{\text{amu}}$ corresponding to a rotational angle reduction of $\sim 1.6°$, the excited mode amplitude is insufficient to drive the magnetic transition. In order to dynamically achieve it, one should either increase the laser intensity or reduce the critical rotation angle through additional means. We discuss both options in the next section.

IV. DISCUSSION

A. Critical intensity for the magnetic transition

First, we assess the relationship among the laser parameters and the resulting driven-mode amplitude to understand how strongly the mode should be driven to achieve the dynamical magnetic transition. Fig. 5 shows the stationary nonequilibrium displacements (damping is neglected) of the $A_g\,(25)$ mode as a function of the laser intensity for different pump frequencies. At low laser intensity, a higher frequency pump induces a larger displacive amplitude of the Raman mode whereas lower pump frequencies lead to larger maximum displacements Fig. 5. The reason for this behavior at low-laser intensity is due to the renormalized frequency of the IR mode being close to that of its eigenfrequency, $\tilde{\nu}_{IR} \approx \nu_{IR}$. Then the pumped IR amplitude, as well as the driven displacive Raman amplitude, increase proportionally to the laser intensity. However, in the high-intensity limit, the renormalized frequency of the IR mode is red-shifted according to the nonlinear coupling. When the renormalized IR frequency $\tilde{\nu}_{IR}$ is close to the pump laser frequency ω, the IR mode is pumped resonantly, which dramatically increases the mode amplitude. In this case, beating-type vibrational dynamics result between the IR and the Raman mode with the maximum displacive Raman mode found at resonance. Because the resonance condition is reached at a higher pump intensity for a lower pump laser frequency, the maximum Raman amplitude will then be larger than that induced by a higher pump frequency.

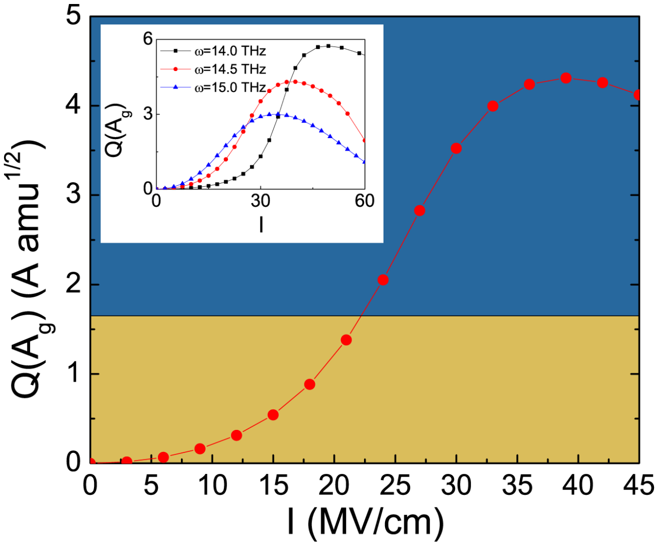

FIG. 5. Mode amplitude $Q(A_g)$ as a function laser intensity ($\omega = 14.5\,\text{THz}$). Different colors denote different magnetic order as in Fig. 1. The inset shows the same quantity for different pump frequencies.

Over all, we find that the estimated critical laser intensity from Fig. 5 with $\omega = 14.5$ THz is ∼22 MV/cm. Note that the optical pump-probe procedure transfers energy to the electronic system, which heats the sample. It should be experimentally more desirable then to reduce the critical rotation angle required rather than increase the pump intensity.

B. Strain to reduce the critical intensity

Here we propose to impose static epitaxial strain on a YTO thin film grown on a (110)-oriented substrate. This mechanical constraint is based on the fact that both the rotation and tilt angle should be reduced to bring the material close to the phase transition point. If the sample is strained in the conventional [001] orientation, the changes in the rotation and the tilt angles exhibit opposite behavior and effectively cancel: For compressive (tensile) strains, the rotation angle increases (decreases) while the tilt angle decreases (increases). If the sample is grown on a (110)-oriented substrate, and strain is applied

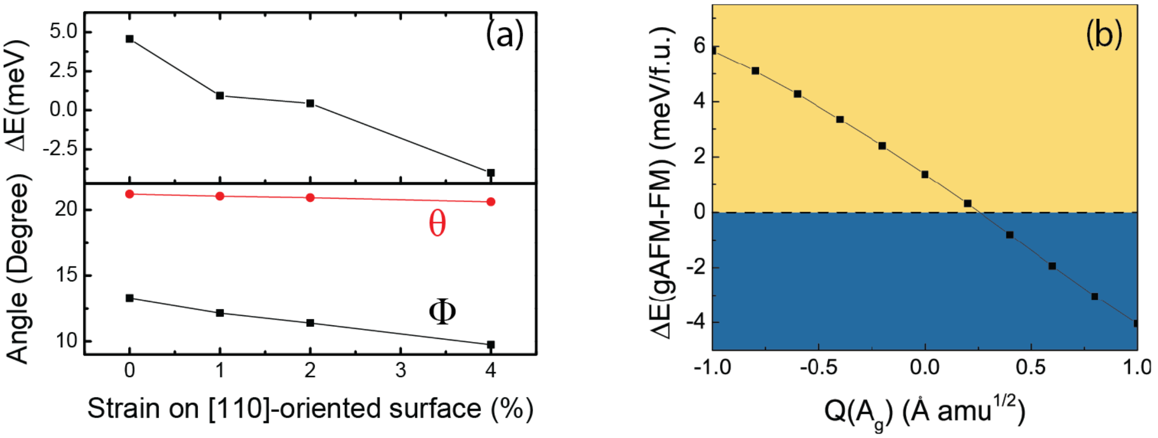

FIG. 6. (a)Energy difference between the FM and G-AFM phases (upper panel) and the rotation and tilt angles with respect to strain (lower panel). (b) The energy difference between G-AFM and FM phases as a function of the amplitude of the A_g (24) mode under ∼2% strain. The different background colors denote the stable magnetic ordering as specified in Fig. 1.

TABLE IV. One-to-one correspondence among phonon modes for bulk and strained $YTiO_3$ on (110) $KTaO_3$.

Bulk $YTiO_3$				$YTiO_3$ film strained on (110) $KTaO_3$			
Band #	Character	ν	g	Band #	Character	ν	g
25	A_g	298	-	24	A_g	279	-
48	B_{1u}	511	-0.04	51	B_u	502	-0.04
53	B_{3u}	532	0.02	52	A_u	508	-
54	B_{1u}	543	0.05	50	A_u	487	-
56	B_{2u}	554	0.008	53	B_u	513	-
57	B_{1u}	561	0.006	58	B_u	577	0.003

along [111] and [1$\bar{1}$1] directions (in terms of pseudo-cubic axes), then both the rotation and tilt angles will decrease or increase together.[42] Indeed for YTO, we find both angles decrease almost linearly when tensile strain is applied Fig. 6 (a). The energy difference between the FM and G-AFM phase is only 0.4 meV/f.u. at a tensile strain of 2%, suggesting a substrate lattice constant of approximately 3.98 Å would be the best option.

Next we compute the lattice dynamical properties and the nonlinear phononic coupling for YTO under such strain condition. Note that the epitaxial constraint of the (110) substrate reduces the crystal symmetry to $P2_1/m$. Therefore, the character and frequency of the phonon modes change accordingly. Nonetheless, a one-to-one correspondence can be identified between the bulk and the new phonon modes by examining the distortion patterns (Table IV). We find the phonon frequencies for most modes decrease except the highest frequency B_u (58) mode. The bulk A_g (25) mode is mapped onto the A_g (24) mode with frequency $\nu = 279$ cm^{-1}. We checked the energy difference between the FM and G-AFM as a function of this A_g (24) mode. Fig. 6 (b) shows the A_g (24) mode for the 2%-strained YTO, further confirming that this mode is the most effective A_g mode to activate the magnetic transition. The critical amplitude for the FM to G-AFM phase transition is reduced to only ∼ 0.25 Å$\sqrt{\text{amu}}$.

We also computed the coupling coefficient for the mode pair of interest, $[A_g(24), B_u(51)]$, and found that it is almost unchanged for strained $YTiO_3$. With this coupling coefficient and the change in crystal structure under the strain state, the predicted critical laser intensity for the phase transition is ∼ 13.1 MV/cm, reduced by 40 %. These features make $KTaO_3$ ($a \sim 3.988$ Å) a good candidate to grow YTO films on and attempt the magnetophononic experiment.

C. Multi-mode excitations

Another possible route to reduce the critical rotation angle is to consider the excitation of a Jahn-Teller-type (JT) Raman mode. This mode is closely related to orbital occupation and magnetic ordering;[40] therefore, it could dynamically bring the system closer to the phase boundary. Such a JT mode should be simultaneously excited through the nonlinear phononic coupling when symmetry allowed. To assess this effect, we computed the energies for the FM, G-AFM, and A-AFM phases as functions of the A_g (25) mode amplitude in a background of the $Q[A_g(49)] = 0.2$ Å$\sqrt{\text{amu}}$, which corresponds to the driven amplitude at the FM-to-G-AFM transitions (Fig. 7). The frequency of this mode (512 cm^{-1}) is very close to the pump frequency and therefore its amplitude could be resonantly enhanced.

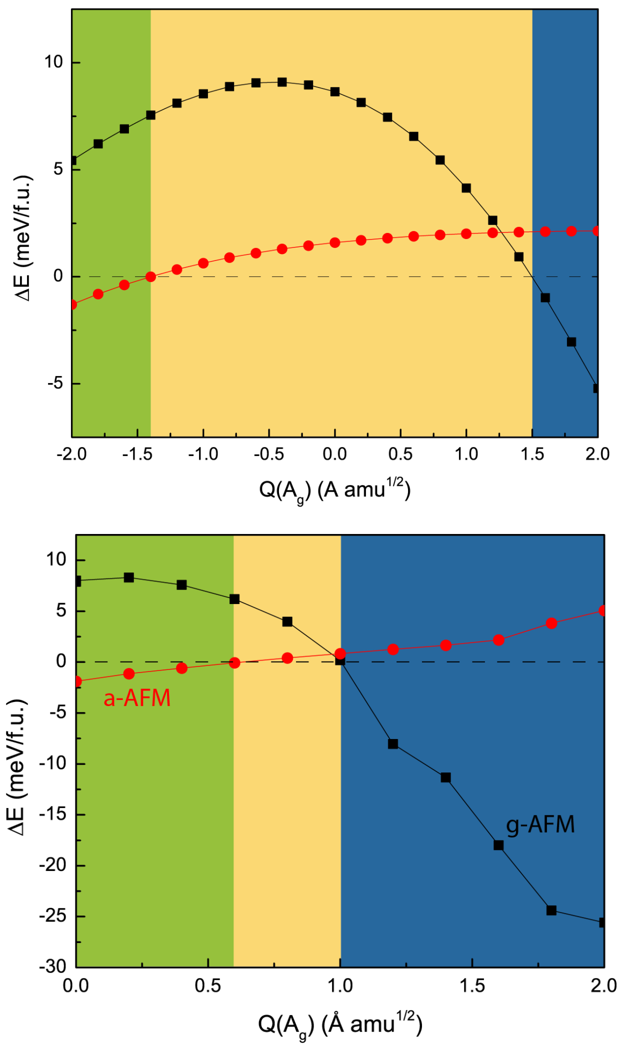

FIG. 7. The energy difference between G-AFM (black) or A-AFM (red) and the FM spin order as a function of the amplitude of the A_g (25) Raman mode in a background of (upper) 0.2 Å$\sqrt{\text{amu}}$ and (lower) 1 Å$\sqrt{\text{amu}}$ of the JT distortion. The different background colors denote the stable magnetic ordering as specified in Fig. 1 of the main text.

The upper panel of Fig. 7 shows the stabilities of the FM, G-AFM and A-AFM phases with the background amplitude of the assisting JT mode being 0.2 Å$\sqrt{\text{amu}}$. Now the hidden A-AFM phase is more stable then the FM phase when the $A_g(25)$ mode has a negative amplitude of $\sim$ 1.4 Å$\sqrt{\text{amu}}$. To access this region one should consider pumping the $B_{1u}(54)$ mode, which has an opposite displacement, with the frequency of $\sim$ 16.3 THz. When $Q[A_g(25)] > 1.5$ Å$\sqrt{\text{amu}}$, the G-AFM state is more stable. Both required amplitudes for the phase transition are reduced from their values based on the original IR-Raman coupling in the absence of the Q$_2$ Jahn-Teller mode.

The A-AFM phase is accessible under the background Q_2 Jahn-Teller mode owing to this JT mode exhibiting the two-in–two-out type of distortion for the equatorial oxygen atoms. Such distortion is the active mode in A-AFM LaMnO$_3$. Here, the d^1 electron prefers to occupy the d_{xz}/d_{yz} orbital in an alternating pattern between neighboring Ti sites similar to the alternating orientation of the d_{z^2} orbital in the e_g manganite system. In this way, the previously hidden A-AFM phase can be accessed with a NLP excitation.

The lower panel of Fig. 7 shows the stabilities of the FM, G-AFM and A-AFM phases with a larger background amplitude of the assisting JT mode being 1 Å$\sqrt{\text{amu}}$. For small $Q[A_g(25)]$, ranging from 0 to 0.7 Å$\sqrt{\text{amu}}$, the A-AFM state is more stable than the FM state. For larger amplitudes, $Q[A_g(25)] > 1$ Å$\sqrt{\text{amu}}$, however, the G-AFM state is more stable as the rotation and tilt angle decrease. The FM spin order is found to be intermediate between the two AFM phases when $Q[A_g(25)] = 1$ Å$\sqrt{\text{amu}}$. Under such an extreme JT background, the magnetic transitions occur at much smaller amplitudes of the $Q[A_g(25)]$ mode. Note that although a pure NLP excitation of this JT mode to such an amplitude is not practical, one may induce static JT-like distortions using chemical substitution or superlattice design.

Last, we emphasize the combination of these two approaches can be used to further reduced the required pump intensity to access the hidden A-AFM phase arising in the NLP interaction.

V. CONCLUSION

By considering the structure-property relationship, we have identified the magnetic phase transitions in d^1 titanates. Based on a (quasi-static) Born-Oppenheimer approximation and ground state density functional theory, we proposed the route to drive the phase transition through NLP pump-probe method. The critical intensity is predicted to be 22 MV/cm with a laser frequency of 14.5 THz. Furthermore, we have discussed possible way to reduce the critical intensity. However, there are two technical issues to be solved: First, the high laser intensity may destroy the magnetic state and interactions in the material, considering the critical temperature of YTiO$_3$ is only 30 K. Therefore, one should look for a material with higher magnetic ordering temperature. Second, spin conservation laws will also affect the dynamics across the transitions and they may be lifted by additional interactions, e.g., external magnetic fields, magnetic impurities, or effective fields such as the laser helicity and spin-orbit coupling. The importance of these effects on spin-wave dispersions and transport properties in the transient states requires additional investigation.

ACKNOWLEDGMENTS

The authors thank M. Fechner, R. Averitt, V. Gopalan, and D. Puggioni for fruitful discussions. M.G. and J.M.R. acknowledge financial support from the U.S. Department of Energy (DOE) under Grant No. DE-SC0012375. Calculations were performed using the Extreme Science and Engineering Discovery Environment (XSEDE), which is supported by NSF Grant No. ACI-1548562 and and the CARBON Cluster at Argonne National Laboratory (DOE-BES, Contract No. DE-AC02-06CH11357).

---

[*] jrondinelli@northwestern.edu

[1] M. Först, R. Mankowsky, and A. Cavalleri, Accounts of Chemical Research **48**, 380 (2015).

[2] D. N. Basov, R. D. Averitt, and D. Hsieh, Nat. Mater. **16**, 1077 (2017).

[3] M. Rini, R. Tobey, N. Dean, J. Itatani, Y. Tomioka, Y. Tokura, R. W. Schoenlein, and A. Cavalleri, Nature **449**, 72 (2007).

[4] M. Mitrano, A. Cantaluppi, D. Nicoletti, S. Kaiser, A. Perucchi, S. Lupi, P. Di Pietro, D. Pontiroli, M. Ricco, S. R. Clark, D. Jaksch, and A. Cavalleri, Nature **530**, 461 (2016).

[5] R. Mankowsky, A. Subedi, M. Först, S. O. Mariager, M. Chollet, H. T. Lemke, J. S. Robinson, J. M. Glownia, M. P. Minitti, A. Frano, M. Fechner, N. A. Spaldin, T. Loew, B. Keimer, A. Georges, and A. Cavalleri, Nature **516**, 71 (2014).

[6] R. Mankowsky, A. von Hoegen, M. Först, and A. Cavalleri, Phys. Rev. Lett. **118**, 197601 (2017).

[7] D. M. Juraschek, M. Fechner, and N. A. Spaldin, Physical Review Letters **118**, 054101 (2017).

[8] S. Bhattacharjee, E. Bousquet, and P. Ghosez, Physical Review Letters **102**, 117602 (2009).

[9] C. N. R. Rao, A. K. Kundu, M. M. Seikh, and L. Sudheendra, Dalton Transactions **0**, 3003 (2004).

[10] M. Gu, Q. Xie, X. Shen, R. Xie, J. Wang, G. Tang, D. Wu, G. P. Zhang, and X. S. Wu, Physical Review Letters **109**, 157003 (2012).

[11] J. H. Lee, L. Fang, E. Vlahos, X. Ke, Y. W. Jung, L. F. Kourkoutis, J.-W. Kim, P. J. Ryan, T. Heeg, M. Roeckerath, V. Goian, M. Bernhagen, R. Uecker, P. C. Hammel, K. M. Rabe, S. Kamba, J. Schubert, J. W. Freeland, D. A. Muller, C. J. Fennie, P. Schiffer, V. Gopalan, E. Johnston-Halperin, and D. G. Schlom, Nature **466**, 954 (2010).

[12] S. Wall, D. Prabhakaran, A. T. Boothroyd, and A. Cavalleri, Physical Review Letters **103**, 097402 (2009).

[13] M. Fechner, A. Sukhov, L. Chotorlishvili, C. Kenel, J. Berakdar, and N. A. Spaldin, ArXiv e-prints (2017), arXiv:1707.03216 [cond-mat.str-el].

[14] D. M. Juraschek, M. Fechner, A. V. Balatsky, and N. A. Spaldin, Phys. Rev. Materials **1**, 014401 (2017).

[15] D. M. Juraschek and N. A. Spaldin, Science **357**, 873 (2017).

[16] J. M. Rondinelli, S. J. May, and J. W. Freeland, MRS Bulletin **37**, 261 (2012).

[17] T. F. Nova, A. Cartella, A. Cantaluppi, M. Först, D. Bossini, R. V. Mikhaylovskiy, A. V. Kimel, R. Merlin, and A. Cavalleri, Nat Phys **13**, 132 (2017).

[18] A. Subedi, A. Cavalleri, and A. Georges, Phys. Rev. B **89**, 220301 (2014).

[19] E. Pavarini, A. Yamasaki, J. Nuss, and O. K. Andersen, New Journal of Physics **7**, 188 (2005).

[20] Y. Okimoto, T. Katsufuji, Y. Okada, T. Arima, and Y. Tokura, Physical Review B **51**, 9581 (1995).

[21] J. P. Goral and J. E. Greedan, Journal of Magnetism and Magnetic Materials **37**, 315 (1983); J. E. Greedan, Journal of the Less Common Metals **111**, 335 (1985).

[22] B. Keimer, D. Casa, A. Ivanov, J. W. Lynn, M. v. Zimmermann, J. P. Hill, D. Gibbs, Y. Taguchi, and Y. Tokura, Physical Review Letters **85**, 3946 (2000).

[23] D. Khomskii, *Transition metal compounds* (Cambridge University Press, Cambridge, 2014).

[24] M. Mochizuki and M. Imada, Phys. Rev. Lett. **91**, 167203 (2003); Journal of the Physical Society of Japan **70**, 1777 (2001); Journal of the Physical Society of Japan **70**, 2872 (2001); A. Filippetti, C. D. Pemmaraju, S. Sanvito, P. Delugas, D. Puggioni, and V. Fiorentini, Phys. Rev. B **84**, 195127 (2011).

[25] X. Huang, Y. Tang, and S. Dong, Journal of Applied Physics **113**, 17E108 (2013).

[26] G. Kresse and J. Furthmuller, Computational Materials Science **6**, 15 (1996).

[27] G. Kresse and D. Joubert, Phys. Rev. B **59**, 1758 (1999).

[28] P. E. Blöchl, Phys. Rev. B **50**, 17953 (1994).

[29] M. Ropo, K. Kokko, and L. Vitos, Phys. Rev. B **77**, 195445 (2008).

[30] A. Togo and I. Tanaka, Scr. Mater. **108**, 1 (2015).

[31] S. L. Dudarev, G. A. Botton, S. Y. Savrasov, C. J. Humphreys, and A. P. Sutton, Physical Review B **57**, 1505 (1998).

[32] I. Solovyev, N. Hamada, and K. Terakura, Physical Review B **53**, 7158 (1996).

[33] M. Gu and J. M. Rondinelli, Phys. Rev. B **95**, 024109 (2017).

[34] M. Eitel and J. E. Greedan, Journal of the Less Common Metals **116**, 95 (1986).

[35] H. Xiang, C. Lee, H.-J. Koo, X. Gong, and M.-H. Whangbo, Dalton Transactions **42**, 823 (2013).

[36] I. V. Solovyev, Phys. Rev. B **69**, 134403 (2004).

[37] A. T. Zayak, X. Huang, J. B. Neaton, and K. M. Rabe, Physical Review B **74**, 094104 (2006).

[38] J. Zaanen and G. A. Sawatzky, Canadian Journal of Physics **65**, 1262 (1987).

[39] R. Mankowsky, M. Först, T. Loew, J. Porras, B. Keimer, and A. Cavalleri, Physical Review B **91**, 094308 (2015).

[40] H. Sawada, Y. Morikawa, K. Terakura, and N. Hamada, Phys. Rev. B **56**, 12154 (1997).

[41] M. Fechner and N. A. Spaldin, Phys. Rev. B **94**, 134307 (2016).

[42] J. M. Rondinelli and N. A. Spaldin, Advanced Materials **23**, 3363 (2011).